Inorganic Chemistry

ARTICLE

pubs.acs.org/IC

Theoretical Insights into the Magnetostructural Correlations in Mn_3-Based Single-Molecule Magnets

M. Atanasov,[*,†,‡,§] B. Delley,[*,†] F. Neese,[*,§] P. L. Tregenna-Piggott,[†,∥] and M. Sigrist[⊥,¶]

[†]Paul Scherrer Institute and ETH Zürich, CH-5232 Villigen PSI, Switzerland

[‡]Institute of General and Inorganic Chemistry, Bulgarian Academy of Sciences, 1113 Sofia, Bulgaria

[§]Lehrstuhl für Theoretische Chemie, Universität Bonn, Wegelerstrasse 12, D-53115 Bonn, Germany

[⊥]Institute Laue Langevin, Avenue des Martyrs, BP 156, F-38042 Grenoble Cedex 9, France

[¶]Institute of Chemistry, Universitetsparken 5, DK-2100 Copenhagen, Denmark

Supporting Information

ABSTRACT: Density functional theory (DFT) and the valence bond configuration interaction (VBCI) model have been applied to the oximato-based $Mn^{III}{}_3O$ single-molecule magnets (SMMs), allowing one to correlate the $Mn^{III}-Mn^{III}$ exchange coupling energy (J) with the bridging geometry in terms of two structural angles: the Mn−O−N−Mn torsion angle (γ) and the Mn_3 out-of-plane shift of O (angle $\delta\theta$). Using DFT, a two-dimensional (γ, $\delta\theta$) energy surface of J is derived and shown to yield essentially good agreement with the reported J values deduced from magnetic susceptibility data on trigonal oximato-bridged Mn_3 SMMs. VBCI is used to understand and analyze the DFT results. It is shown that the exchange coupling in these systems is governed by a spin-polarization mechanism inducing a pronounced and dominating ferromagnetic exchange via the oximato bridge as opposed to kinetic exchange, which favors a weaker and antiferromagnetic exchange via the bridging oxide. In the light of these results, a discussion of the exchange coupling in the Mn_6 family of the SMM with a record demagnetization barrier is given.

I. INTRODUCTION

The aim of this work is a theoretical understanding of the magnetic properties and exchange couplings in the Mn_3-based family of single-molecule magnets (SMMs). Specifically, we seek an explicit connection between the sign and magnitude of the exchange coupling energy (J) as a function of the bridging ligand geometry.

An appreciable amount of work, since the discovery of the first SMM, $[Mn_{12}O_{12}(CH_3COO)_{16}(H_2O)_4]\cdot 2CH_3COOH\cdot 4H_2O$,[1−4] has been devoted to the synthesis and characterization of magnetic clusters with SMM features: in particular, the slow relaxation (blocking) of the magnetization. This feature could eventually lead to use of these molecules for information storage and quantum computing at the molecular level.

The property of a compound behaving as a SMM stems from the combination of a spin $S > {}^1/_2$ ground state (implying ferromagnetic or uncompensated antiferromagnetic couplings) and an uniaxial magnetic anisotropy (D). In the Mn^{III}-based SMM, the magnetic anisotropy is intrinsically related to the local (single-ion) anisotropies originating from the Jahn−Teller distorted octahedral Mn^{III} building blocks, which may eventually result in a negative zero-field-splitting parameter D for the entire cluster. An energy barrier for the reversal of the magnetization U proportional to D emerges.

The first ferromagnetic $[Mn^{III}{}_3O]^{7+}$ triangle, $[Mn_3O(bamen)](ClO_4)$ [H2bamen = 1,2-bis(biacetylmonoximeimino)ethane], was reported in 2002.[5] A dominant ferromagnetic exchange was discovered in three Mn/carboxylato/oximato complexes, $[Mn^{III}{}_3O(O_2CR)(mpko)_3](ClO_4)$ [R = Me (**1**), Et (**2**), Ph (**3**); mpko = methyl 2-pyridyl ketone oximato],[6−8] and this evolved following the synthesis and characterization of a series of analogous Mn_3 and Mn_6 SMM compounds, derived when replacing the mpko ligand with salicylaldoxime ($saoH_2$) or its "bulkier" cousins Me(Me-$saoH_2$), Et (Et-$saoH_2$), and Ph(Ph-$saoH_2$).[9−12] These molecules are derived from the basic carboxylates $[Mn^{III}{}_3O(O_2CR)_6L]^+$ (R = Me, Et, Ph; L = H_2O, py, MeCN, etc.], where the bridging carboxylates (Mn−O−C−O−Mn) have been replaced with bridging oximes (Mn−N−O−Mn), all six in $[Mn_3O(bamen)](ClO_4)$ and only the lower three in **1**−**3** (see ref 13 for a review). The record Mn_6 SMM with a barrier of $U = 86.4$ K[10] can be described (Figure 1) as consisting of two $[Mn^{III}{}_3(\mu_3\text{-}O)]^{7+}$ triangular subunits linked via two "central" oximato O atoms, thus leading to a $[Mn^{III}{}_6(\mu_3\text{-}O)_2(\mu_3\text{-}ONR)_2(\mu_2\text{-}ONR)_4]^{2+}$ core. The bridging between neighboring Mn ions within each triangle occurs through an NO oximato group, such that each Mn_2 pair forms a −Mn−N−O−Mn− moiety and thus a Mn_3 triangle, a $(-Mn-O-N-)_3$ ring. In fact, 24 molecules of this type have been reported,[12] and 6 of them were carefully analyzed in a later study using density functional theory (DFT) on the basis of their experimentally known molecular structures.[14]

While the Mn_3-Mn_3' exchange linking two Mn_3 triangles is found invariably to be ferromagnetic (Mn−O−Mn bridging angles are close to 90°; Figure 1), the type of Mn−Mn coupling

Received: June 1, 2010
Published: February 18, 2011

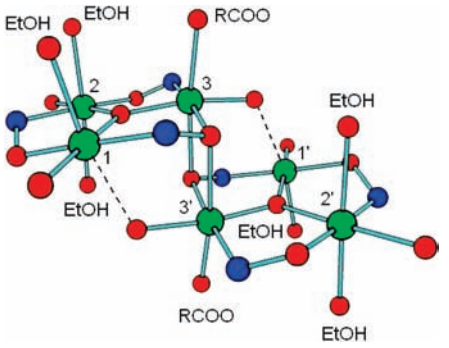

Figure 1. Basic structural motif and numbering of Mn^{III} paramagnetic centers of the Mn_6 SMM. Color code: Mn^{III}, green; O, red; N, blue. The C and H atoms have been omitted for clarity. The weak axial interactions between the phenolate O atoms and neighboring Mn^{III} ions are indicated by broken lines.

within the triangles varies with the value of the dihedral angle Mn−N−O−Mn (γ). Larger (smaller) values of γ are found both by experiment and by theory (DFT) to correlate with ferromagnetic (antiferromagnetic) exchange couplings.[14]

In addition to γ, the shift of the μ_3-oxo ligand from the Mn_3 plane quantified by deviation of the polar angle θ from 90° (planar structure), $\delta\theta$, is expected to affect the exchange, but in contrast to γ, its effect on Mn−Mn magnetic exchange was regarded as less pronounced.[15]

Analysis of the exchange coupling energies from DFT calculations on **1** and on the analogous system $[Mn_3O(sao)_3(O_2CR)(H_2O)(py)_3]$ [R = Me (**4**), Ph (**5**)][15] has shown a clear correlation of the exchange coupling with another structural parameter: the nonplanarity of the Mn_3O core, τ, which may be quantified by the dihedral angle formed by the $Mn-O_{oxide}-O_{oxime}$ and $Mn-O_{oxime}-N$ planes. Ferromagnetic (antiferromagnetic) couplings were found for **1**−**3** (**4** and **5**) possessing large (small) values of τ. A recent DFT[16] study extended the analysis to other Mn_3O systems and has shown that the distortions described by the angle τ are rather complex and affect not only the exchange (i.e., an effect described by γ) but also the alignment of the Jahn−Teller axes (i.e., misalignment increasing with τ, which reduces the magnetic anisotropy, $|D|$). Thus, depending on the way a given value of τ is obtained (there are three different ways to distort this angle),[16] it was shown that it is, in principle, possible to achieve a geometry in which both ferromagnetic J and negative D are large. However, because of the complexity of this structural parameter and because the chosen systems possess quite different coordination geometries and attached groups, no clear quantitative measure of the effect of the geometry on the magnetic exchange could be achieved so far.

From a more general perspective, exchange coupling and magnetic anisotropy of Mn^{III}-based SMMs have been treated using DFT with the aim of making predictions of the spin Hamiltonian (SH) parameters on the basis of the building blocks.[17−21] In addition, a somewhat rough but qualitatively to semiquantitatively correct ligand-field modeling of the same properties has been demonstrated.[22,23]

It is the aim of the present work to study the magnetostructural correlations in Mn_3O SMMs by combining the numerical results as provided by DFT and the semiempirical valence bond configuration interaction (VBCI) model, which will be used to analyze and understand the DFT results. When the VBCI model is employed,[24−30] rough but correct and general (system-independent)

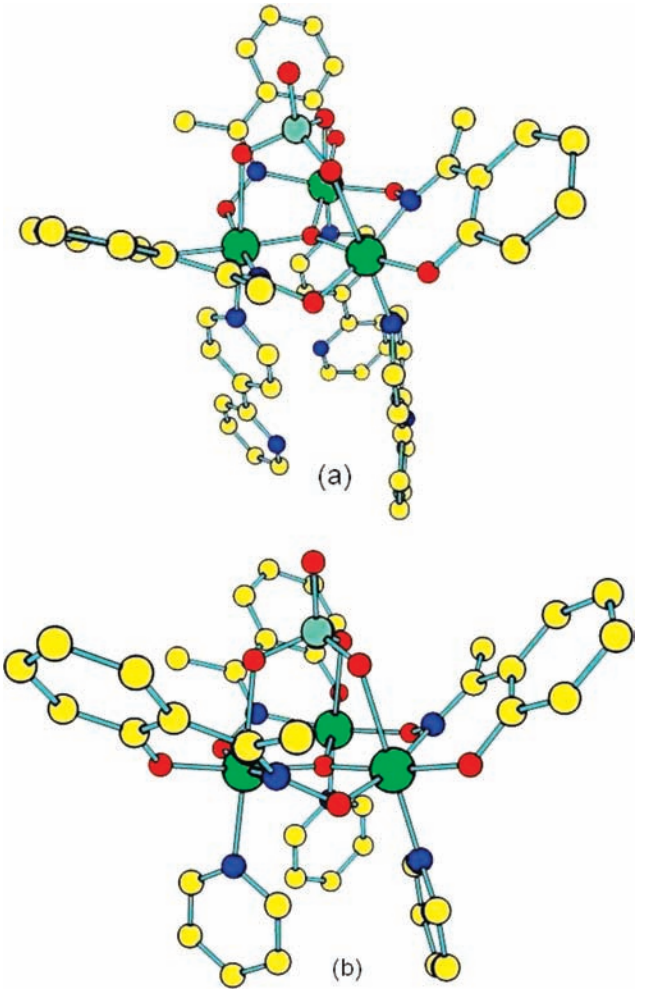

Figure 2. Structures of (a) $[Mn^{III}_3O(Me\text{-}sao)_3(2,4'\text{-}bpy)_3ClO_4]$ (model 1) and (b) its truncated analogue $[Mn^{III}_3O(Me\text{-}sao)_3py_3ClO_4]$ (model 2). Color code: Mn^{III}, green; O, red; N, blue; C, yellow; Cl, light blue. The H atoms have been omitted for clarity.

expressions of the exchange coupling energy J on the angles γ and $\delta\theta$ will be derived. This model has been applied to the magnetic exchange across the cyanide bridge,[26] and its utility to study ground- and excited-state exchange coupling energies in binuclear transition-metal complexes has been repeatedly demonstrated.[27,28] Rather than including complications (such as those encountered in complexes **1**−**5** as well as other Mn_3 compounds[16] or in the Mn_6 SMM) due to the *simultaneous presence of oxime and carboxylate* groups as bridging ligands, we select in this study only Mn_3O molecules in which *solely oxime and oxide* are linking each Mn−Mn pair. Restricting attention further to Mn_3O clusters with trigonal symmetry, we ensure reliable values of J to be obtained from reported magnetic susceptibility data and to be used further to validate the theoretical results.[31] This study has been inspired by a Mn_3O complex, reported recently,[32] $[Mn_3O(Me\text{-}sao)_3(2,4'\text{-}bpy)_3ClO_4]$ (**III**) with an appreciable value of γ = 44.15° and a ferromagnetic Mn_1-Mn_2 (J = 7.1 cm^{-1}, $H_{exc} = -J\hat{S}_1\cdot\hat{S}_2$) coupling (Figure 2), which we studied by inelastic neutron scattering and high-field high-frequency electron paramagnetic resonance. Spectroscopic results will be reported and analyzed separately. In addition to **III**, three other closely related complexes with the same bridging

dx.doi.org/10.1021/ic1023482 |*Inorg. Chem.* 2011, 50, 2112–2124

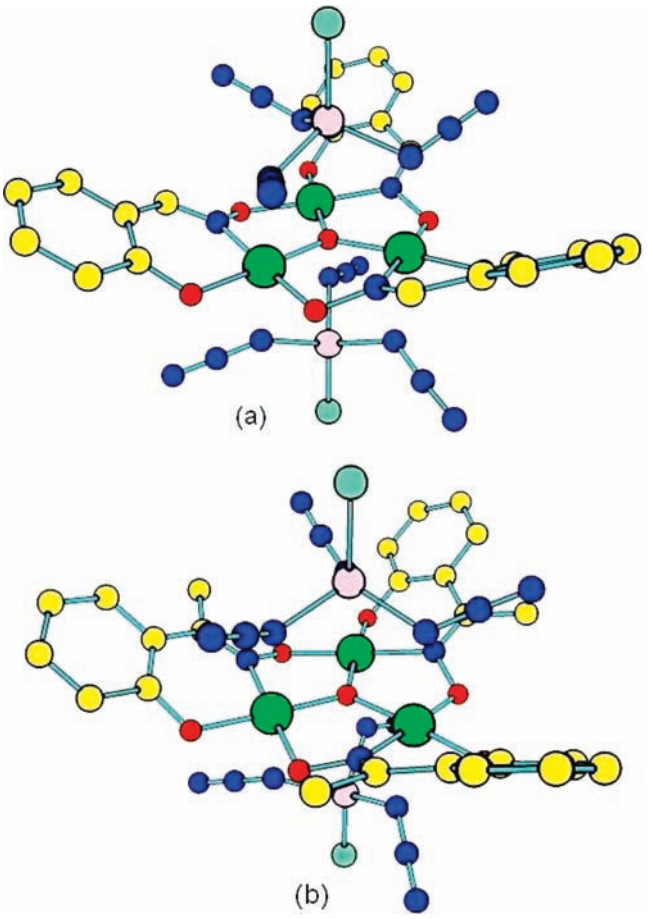

Figure 3. Structures of (a) $[Mn_3Zn_2(H\text{-sao})_3O(N_3)_6X_2]$ (**V**−**VII**; X = Cl, Br) and (b) $[Mn_3Zn_2(Me\text{-sao})_3O(N_3)_6Cl_2]$ (**VIII**). Color code: transition metal Mn, green; transition metal Zn, magenta; O, red; N, blue; C, yellow; halogen, light blue. The H atoms have been omitted for clarity.

topology but different γ and J values, $[Mn_3O(R\text{-sao})_3Y_3ClO_4]$ [R = Naphth, Y = py (**I**), γ = 4.1°, J = −6.20 cm^{-1};[33] R = H, Y = Etpy (**II**) γ = 13.11°, J = −6.04 cm^{-1}, and R = Et, Y = Etpy (**IV**), γ = 46.80°, J = 8.2 cm^{-1}],[13]] and four other trigonal complexes, $[Mn_3Zn_2O(R\text{-sao})_3(N_3)_6X_2](cation)_3$ [R = H, X = Cl, cation = $AsPh_4$ (**V**), γ = 11.93°, J = −8.2 cm^{-1}; R = H, X = Cl, cation = NEt_4 (**VI**), γ = 32.05°, J = 4.8 cm^{-1}; R = H, X = Br, cation = NEt_4 (**VII**), γ = 32.08°, J = 4.6 cm^{-1}; R = Me, X = Cl, cation = NEt_4 (**VIII**), γ = 36.10°, J = 9.4 cm^{-1}][34] (Figure 3), will be included in the analysis. Finally, the exchange coupling energies in Mn_6 will be discussed and some predictive concepts of importance for further development formulated.

II. DFT CALCULATIONS

II.1. DFT Computations. Spin-unrestricted DFT calculations of the exchange coupling energies have been performed with two programs: the DFT all-electron program *DMol*[3] using a double-numerical polarized basis set[35] along with the exchange-correlation potentials DB97 (available in *DMol*[3]) and, for the sake of comparison with the classical Kohn−Sham (KS) method,[36] the Perdew−Becke−Enzerhof (PBE)[37] and Perdew−Wang (PW) correlation[38] functionals (Table S1 in the Supporting Information). For geometries obtained from full and constrained geometry optimizations, the local density approximation in the form of the Vosko, Wilk, and Nusair (LDA-VWN) parametrization of the electron gas data[39] was found from earlier studies to reproduce metal−ligand−metal bridging bonds of importance for magnetic exchange in better agreement with the experiment than with what generalized gradient approximation (GGA) functionals typically give,[40−42] and hence it was used here (see refs 43 and 44 for recent developments).

DFT calculations of the exchange coupling on the basis of the popular B3LYP functional[45] were done with the *ORCA* program package.[46] Calculations have been done on gas-phase isolated Mn_3 complexes and for the highly negatively charged compounds (**V**−**VIII**; net charge 3−) additionally with charge compensation using the conductor-like screening model (COSMO).[47] To speed up calculations of the Mn_3 magnetic clusters with more than 100 atoms, the recently proposed resolution of identity (RI) "chain-of-spheres exchange (COSX)" (RICOSX) algorithm,[48] together with the split-RI-J procedure[49] (a density-fitting variant) for computation of the Coulomb matrix, were used. The COSX algorithm is closely related to Friesner's pseudospectral approach.[50] The exchange coupling constants computed with the RIJCOSX approach were found to be indistinguishable from those computed without this approximation. In these calculations, fairly large contracted basis sets for Mn (16s4p4d3f4g contracted to 6s4p2d3f2g, pattern {1021111/1111/31/111/31}), C, N, and O (8s3p3d1f contracted to 6s3p3d1f, pattern {311111/111/111/1}), and H (4s2p contracted to 2s1p, pattern {31/2}) have been used.[51,52] These basis sets contain higher angular momentum polarization functions than the double-numerical basis set used in the *DMol*[3] calculations. Nevertheless, in cases where comparison is possible (e.g., for the PBE functional), the two programs yield J values within 10% of each other.

II.2. Deducing the Function $J(\gamma,\delta\theta)$ from DFT Calculations. To extract exchange coupling energies from DFT calculations, we made use of the SH of eq 1 and the broken-symmetry approach by Noodleman et al.[53,54] It has been shown that this approach also accounts for, on a firm first-principle basis, both charge-transfer (spin-delocalization) and spin-polarization effects.[54] The J value of a trigonal Mn_3 cluster ($J_{12} = J_{13} = J_{23} = J$) has been deduced from the DFT energies of two calculations: the high-spin $|HS = M_{s1}, M_{s2}, M_{s3}\rangle = |2,2,2\rangle$ and the broken-spin $|BS\rangle = |2, 2, -2\rangle$ Slater determinants.

$$\hat{H}_{exc} = -J_{12}(\hat{S}_1\cdot\hat{S}_2 + \hat{S}_1\cdot\hat{S}_3 + \hat{S}_2\cdot\hat{S}_3) \quad (1)$$

While the first is close to the pure spin S = 6 state, $|BS\rangle$ is not but can be written as the following linear combination of pure spin states $|S, M_s\rangle$ of the entire Mn_3 complex:

$$|BS> = \frac{1}{3\sqrt{55}}|6,2> + \frac{1}{3\sqrt{5}}|5,2> + \sqrt{\frac{6}{55}}|4,2> + \frac{1}{3}\sqrt{\frac{14}{5}}|3,2> + \frac{\sqrt{5}}{3}|2,2> \quad (2)$$

In trigonal symmetry, the energy $E(S)$ is given by the method of Kambe simply as[55]

$$E(S) = -JS(S+1)/2 \quad (3)$$

dx.doi.org/10.1021/ic1023482 |*Inorg. Chem.* 2011, 50, 2112–2124

Table 1. Bond Distances (Å) and Specific Angles (deg) of III from X-ray Data (exp) in Comparison with Their Values Obtained from Geometry Optimizations Using the Large (Model 1) and Smaller $[Mn^{III}_3O(Me\text{-}sao)_3(py)_3ClO_4]$ (Model 2) Clusters with Trigonal Symmetry[a]

	model 1			model 2	
		LDA-VWN functional		LDA-VWN functional	
	exptl X-ray[32]	full opt.	constrained opt.	full opt.	constrained opt.
γ	44.15	46.58	45.15	45.33	44.15
$\delta\theta = 90 - \theta$	8.1	10.95	8.1	11.34	8.1
$R_{Mn-N_{py}}$	2.263	2.213	2.202	2.235	2.207
$R_{Mn-O_{oxide}}$	1.899	1.894	1.882	1.894	1.888
$R_{Mn-O_{oxime}}$	1.908	1.900	1.967	1.901	1.900
$R_{Mn-N_{oxime}}$	1.984	1.967	1.899	1.968	1.966
$R_{Mn-O_{phen}}$	1.857	1.857	1.857	1.855	1.857
$R_{Mn-O_{ClO3}}$	2.556	2.323	2.404	2.319	2.392
∠JT-axis	25.89	27.72	25.83	26.96	26.59
∠JT-C_3	15	16.06	15.0	16.00	15.37
J_{DB97}	13.43	8.37	5.98	13.47	8.35
J_{B3LYP}	6.45	5.62	5.99	6.66	6.72

[a] Mn−Mn exchange coupling energies (cm^{-1}, J_{DB97}) calculated using the given geometries and the DB97 functional are also included.

yielding for $E(HS)$ and $E(BS)$ eqs 4, 5, and, therefore, 6 for J.

$$E(HS) = -21J \quad (4)$$

$$E(BS) = -5J \quad (5)$$

$$J = [E(BS) - E(HS)]/16 \quad (6)$$

The parameter J is a complex function of the angles γ and $\delta\theta$, which define the bridging geometry, and other geometrical parameters not directly involved in magnetic exchange. Thus, variations of the angles $\delta\theta$ and γ will be accompanied with concerted changes of the bond distances to the N- and O-bridging ligands, and even subtle changes of the geometry of the next-nearest neighbors might have an effect on J. In order to obtain J as a smooth function of γ and $\delta\theta$ [denoted by $J(\gamma,\delta\theta)$], we adopt the following approach: Starting with the reported geometry of **III**, i.e., $\gamma = 44.15°$ and $\delta\theta = 8.1°$, we have reduced these values in equidistant steps, thus creating a 6×6 $(\gamma, \delta\theta)$ grid with $\gamma = 0$, 9.13, 18.29, 27.38, 36.64, and 45.86° and $\delta\theta = 0.0$, 1.6, 3.21, 4.82, 6.43, and 8.10°. For each of these 36 $(\gamma, \delta\theta)$ pairs, a constraint DFT optimization has been done by fixing $(\gamma, \delta\theta)$ and relaxing all other geometrical parameters. This was followed by the calculation of J for that $(\gamma, \delta\theta)$ geometry. In doing so, it was possible to map the dependence of J on the bridging geometry onto just the angles γ and $\delta\theta$. Values of $J_{XCP}(\gamma,\delta\theta)$, calculated using different exchange-correlation potentials (XCP), are listed in Table S1 in the Supporting Information. Using these data sets, values of J at intermediate (γ and $\delta\theta$) angles were calculated via interpolation using the polynomial of eq 7 (see Table S2 in the Supporting Information with values of a_i, where $i = 0-9$; standard deviations between polynomially fitted and DFT values are less than 0.40 cm^{-1}).

In the more complex Mn_6 SMM with an inversion center, a SH with three (eq 8) to four (eq 9) different J parameters is utilized (see the numbering of the Mn centers defined in Figure 1). They have been approximated by employing eq 7 and the values of γ and $\delta\theta$ for each bridge.

$$J(\gamma,\delta\theta) = a_0 + a_1\gamma + a_2(\delta\theta) + a_3\gamma^2 + a_4(\delta\theta)^2 + a_5\gamma(\delta\theta) + a_6\gamma^3 + a_7\gamma^2(\delta\theta) + a_8\gamma(\delta\theta)^2 + a_9(\delta\theta)^3 \quad (7)$$

$$\hat{H}_{exc} = -J_{12}\hat{S}_1\cdot\hat{S}_2 - J_{13}\hat{S}_1\cdot\hat{S}_3 - J_{23}\hat{S}_2\cdot\hat{S}_3 \quad (8)$$

$$\hat{H}_{exc} = -J_{12}(\hat{S}_1\cdot\hat{S}_2 + \hat{S}_{1'}\cdot\hat{S}_{2'}) - J_{13}(\hat{S}_1\cdot\hat{S}_3 + \hat{S}_{1'}\cdot\hat{S}_{3'}) - J_{23}(\hat{S}_2\cdot\hat{S}_3 + \hat{S}_{2'}\cdot\hat{S}_{3'}) - J_{33'}\hat{S}_3\cdot\hat{S}_{3'} \quad (9)$$

III. RESULTS AND DISCUSSION

III.1. Exchange Coupling in Trigonal Mn_3 Clusters from DFT Calculations. The prototype trigonal complex **III** (Figure 2, model 1) consists of an equilateral Mn^{III}_3 triangular core connected by a μ_3-oxo group in the center that lies 0.28 Å ($\delta\theta = 8.1°$) below the Mn_3 plane.[32] The cluster is capped by one ClO_4^- group in a $\eta^1{:}\eta^1{:}\eta^1{:}\mu^3$ coordination mode (model 1, Figure 2a) above this plane and by three 2,4′-bipyridine ligands, forming long Mn^{III}−O and Mn^{III}−N bonds to each Mn^{III} in a trigonal (C_3) arrangement, below the plane. Each edge of the triangle is bridged by a dianionic oximato group of the Me-sao in a $\eta^1{:}\eta^1{:}\eta^1{:}\mu^2$ coordination mode, whose deprotonated phenolate group forms a terminal bond to the corresponding Mn^{III}. An intramolecular $O_{oxime}\cdots H-CH_2$ hydrogen bond (RO···H = 2.2 Å) is responsible for the significant twist of each Mn−N−O−Mn moiety ($\gamma = 44.15°$; see Table 1 for an experimental set of interesting bond lengths and angles). The coordination geometry of each Mn^{III} is that expected for a Jahn−Teller axially elongated Mn^{III} octahedral complex with short bonds that are nearly coplanar with the Mn_3 plane and long Jahn−Teller axes almost parallel to the C_3 axis, thus leading to a $S = 2$ ($d_{yz}^1 d_{xz}^1 d_{xy}^1 d_{z^2}^1$) high-spin ground state at each Mn^{III} center.

A DFT geometry optimization using the LDA-VWN functional leads to Mn−ligand bond distances and angles $\delta\theta$, γ,

dx.doi.org/10.1021/ic1023482 |Inorg. Chem. 2011, 50, 2112–2124

Table 2. Exchange Coupling Energies (cm^{-1}) for Trigonal Mn^{III}_3 SMMs from DFT (J_{B3LYP}) in Comparison with the Experimental Ones[a] (J_{exp}) and with the Structural Angles γ and $\delta\theta$ (deg)

complex	J_{B3LYP}	J_{exp}	γ	$\delta\theta$
$[Mn_3O(Naphth\text{-}sao)_3py_3ClO_4]$ (**I**)[b]	−12.43	−6.20	4.1	6.5
$[Mn_3O(sao)_3(Etpy)_3ClO_4]$ (**II**)[c]	−13.96	−6.04	13.11	8.3
$[Mn_3O(Me\text{-}sao)_3(2,4\text{-}bpy)_3ClO_4]$ (**III**)[d]	6.08	7.1	44.15	8.10
$[Mn_3O(Et\text{-}sao)_3(Etpy)_3ClO_4]$ (**IV**)[c]	6.99	8.20	46.80	8.4
$[Mn_3Zn_2O(sao)_3(N_3)_6Cl_2](AsPh_4)_3$ (**V**)[e]	−10.41 (−10.43)[f]	−8.20	11.93	0.52
$[Mn_3Zn_2O(sao)_3(N_3)_6Cl_2](NEt_4)_3$ (**VI**)[e]	3.02 (3.75)[f]	4.8	32.05	0.88
$[Mn_3Zn_2O(sao)_3(N_3)_6Br_2](NEt_4)_3$ (**VII**)[e]	3.20 (4.04)[f]	4.6	32.08	0.76
$[Mn_3Zn_2O(Me\text{-}sao)_3(N_3)_6Cl_2](NEt_4)_3$ (**VIII**)[e]	6.89 (8.72)[f]	9.4	36.10	0.30

[a] Deduced from a fit to the magnetic susceptibility data. [b] Reference 33. [c] Reference 13. [d] Reference 32. [e] Reference 34. [f] The results for the trianionic Mn_3 complexes obtained using the COSMO model are given in parentheses.

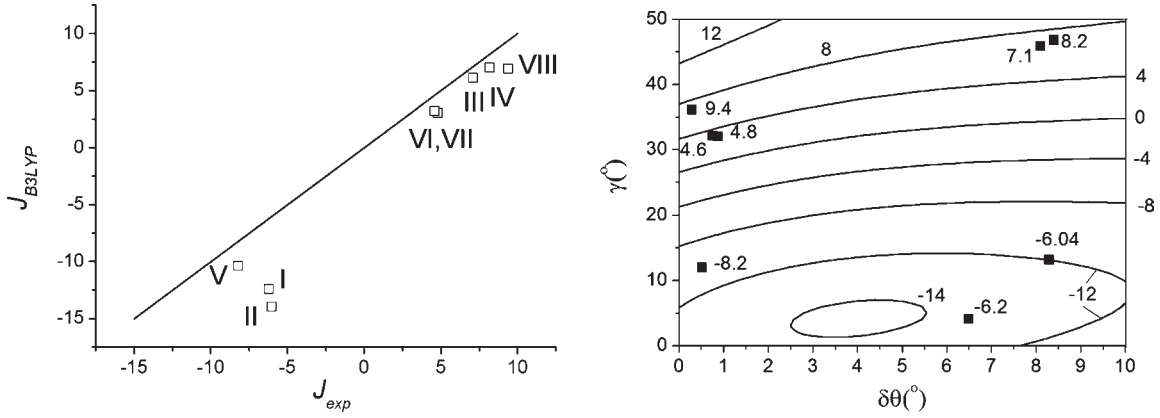

Figure 4. Exchange coupling energies (cm^{-1}) for a trigonal Mn^{III}_3 SMM from DFT (J_{B3LYP}) vs experimental values (J_{exp}) (□), in comparison with a hypothetical ($J_{B3LYP} = J_{exp}$) line of coincidence (left); $J(\gamma,\delta\theta)$ contour plot diagrams for the Mn_3 SMM with trigonal symmetry from constrained DFT geometry optimizations using the B3LYP exchange-correlation potential (eq 7 and Tables S1 and S2 in the Supporting Information). Experimental points for the representatives from Table 2 (■) are listed for the sake of comparison (right).

∠JT-axis (angle between the Jahn−Teller axes), ∠JT-C_3 (angle between the Jahn−Teller and C_3 axes) in good agreement with the experiment. The J values calculated with DB97 (J_{DB97}) and B3LYP (J_{B3LYP}) are also in good agreement with the experiment, provided the DFT-optimized geometries are employed (Table 1; $J_{exp} = 7.1\ cm^{-1}$,[32] compared to $J_{DB97} = 13.43\ cm^{-1}$ based on the experimental geometry). Table 1 also lists structural data and J values from a geometry optimization at fixed experimental values of the angles $\delta\theta$ and γ. Compared with the fully optimized complex, Mn−O_{oxime} (Mn−N_{oxime}) bond lengths are 0.07 Å longer (shorter) and the value of J_{DB97} is 30% lower, manifesting the sensitivity of the exchange coupling with respect to *both* $\delta\theta$ and γ and the metal−ligand bond distances.

Because geometry optimizations for model 1 are very time-consuming, we have chosen a truncated model complex in which the 2,4′-bpy ligand has been replaced by pyridine (py; model 2, Figure 2b). Both the geometries (i.e., the angles $\delta\theta$ and γ and the metal−ligand bond distances) and the exchange coupling energy J remain essentially unaffected by this simplification (Table 1).

In Table 2, we list data for three more complexes (**I**, **II**, and **IV**; see the Introduction) similar to **III** but differing in the bulkiness of their substituents at the R-sao ligand. With the exception of **I**, where because of the aryl nature of the Naphth-sao substituent the Mn_3 oxime unit can be considered nearly planar ($\gamma = 4.11°$), with an increase in R, one observes an increase in γ accompanied with an increase of J_{exp}, which we could well reproduce using the experimental values of γ and $\delta\theta$ and the function $J_{B3LYP}(\gamma,\delta\theta)$ (eq 7).

The trigonal $[Mn_3Zn_2]^{13+}$ magnetic clusters (**V**−**VIII**[34]) possess $[Mn_3{}^{III}(\mu_3\text{-oxo})]^{7+}$ magnetic cores identical with that of **III**, with the only difference being that, instead of the capping ClO_4^- and the three 2,4′-bpy groups, there are six axially bound $\mu\text{-}\eta^1{:}\eta^1$ azido ligands (Figure 3). The Mn−azide bonds lie along the axial Jahn−Teller distortion axes and connect the Mn^{III}_3 core to two tetrahedrally coordinated, nonmagnetic Zn^{II} ions, resulting in almost parallel individual ion Jahn−Teller axes. It is remarkable that here the angle γ varies with the crystal packing as a result of systematic variations in the cocrystallizing cation, the terminal ion, and the R group (R = H, CH_3), while the μ_3-oxo ion lies now almost exactly in the Mn_3 plane (the $\delta\theta$ angles are close to zero). Adopting the experimentally reported values of γ and $\delta\theta$ and $J_{B3LYP}(\gamma,\delta\theta)$ (eq 7), we could reproduce the exchange coupling parameters deduced from magnetic susceptibility data (Table 2 and Figure 4, left), in particular, when charge compensation in the case of the trianions using the COSMO model is taken into account. It is interesting to find out, once more and similar to the data for complexes **I**−**IV**, that the γ angle in the compound containing sao-CH_3 is larger that in the other three complexes possessing the nonsubstituted sao-H ligand, and the value of this angle correlates with the largest reported (and also calculated using B3LYP) J value.

dx.doi.org/10.1021/ic1023482 |*Inorg. Chem.* 2011, 50, 2112–2124

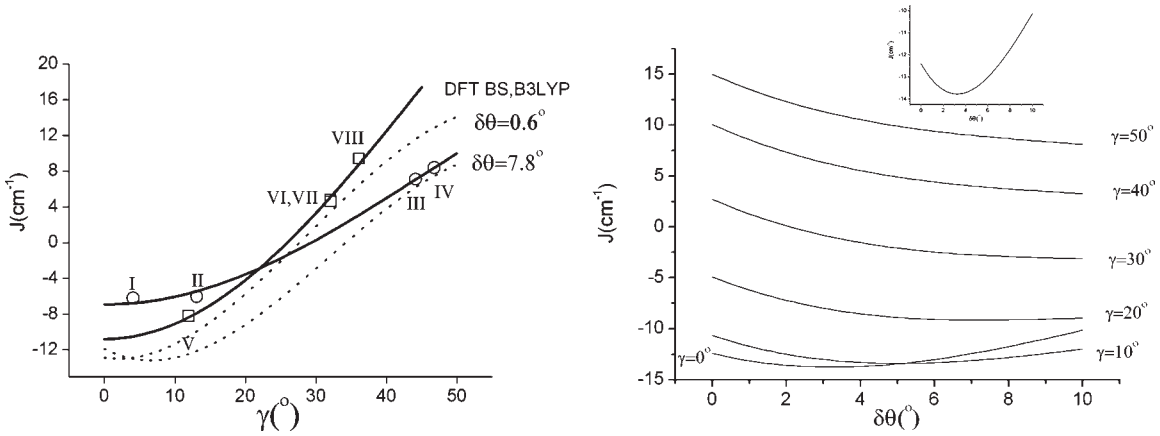

Figure 5. Dependence of the exchange coupling energy on the angle γ resulting from a fit of the parameters J_0 and J_1 of eq 10 to J values from magnetic susceptibility data of **I**−**IV** and **V**−**VIII** (solid line) in comparison with DFT-B3LYP calculations (dotted line, left) and dependence of J on the angle $\delta\theta$ at various fixed values of the angle γ from DFT-B3LYP calculations (right). The inset shows the $J(\delta\theta)$ dependence at a geometry with $\gamma = 0°$.

It follows from a comparison between the DFT calculated (using the same $J_{B3LYP}(\gamma,\delta\theta)$ dependence of eq 7) and experimental J values (Figure 4, left) that the bridging functions of both oxime and oxide in complexes **I**−**IV** and **V**−**VIII** are electronically the same and well accounted for by variations in their angles γ and $\delta\theta$. The latter are determined, in turn, by the specific coordinations that differ essentially between **I**−**IV** and **V**−**VIII** (counterions, terminal ions, and hydrogen bonds; see above). With positive J, a comparison between the results from theory and experiment is perfect, while even with B3LYP, negative J values are too large for antiferromagnetic coupling. It is also interesting to note that, for ferromagnetic couplings, the DB97 functional yields results that are comparable to, if not even better than, the results of the computationally more demanding B3LYP functional (Table S1 and Figure S6 in the Supporting Information).

The data in Table 2 provide the basis for quantitative magnetostructural correlations. A $J_{B3LYP}(\gamma,\delta\theta)$ contour plot diagram (Figure 4, right) shows a nice agreement between the DFT-calculated isolines of J and the experimental points that characterize the complexes in Table 2. In line with previous experimental and DFT results, the exchange coupling energy J is a sensitive and monotonically increasing function of γ (Figure 5, left) but is still (but to a lesser extent) dependent on $\delta\theta$ (Figure 5, right). It is interesting to compare the plot of Figure 4 with results using other functionals, i.e., the KS, PBE, PW91, and DB97 (Figures S3−S6, respectively, in the Supporting Information). While the topology of the isolines in these contour plots remains essentially the same, there is a negative (downward, or antiferromagnetic) shift by about −7, −22, and −36 cm^{-1} when going from B3LYP to the KS, PBE, and PWC functionals, respectively.

On the basis of the reported structural data (Table 2) we can subdivide complexes **I**−**VIII** into two groups according to their values of $\delta\theta$; **V**−**VIII** with almost planar Mn_3O cores ($\delta\theta$ = 0.6 ± 0.3°) and **I**−**IV** with larger deviations of oxide from the Mn_3 plane ($\delta\theta = 7.8 \pm 0.9_5°$). The J vs γ plots for the fixed values of $\delta\theta$ = 0.6 and 7.8° (Figure 5, left) and J vs $\delta\theta$ plots (fixed γ; Figure 5, right) show that for larger γ angles there is a decrease of the ferromagnetic coupling (smaller J) when moving O out of the Mn_3 plane. This is the opposite to what one observes for small γ angles; for such geometries, exchange coupling is antiferromagnetic and goes through a shallow maximum before further decreasing with an increase of $\delta\theta$ (see the inset in Figure 5, right).

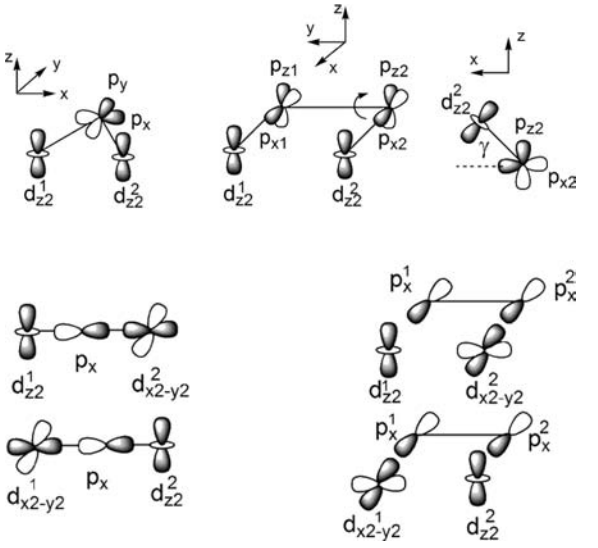

Figure 6. Orbitals involved in the spin−spin exchange mechanism across the Mn−O−Mn (left) and Mn−O−N−Mn bridges (right); orbital interactions including the singly occupied d_{z^2} orbitals of Mn^{III} (top) and the singly occupied d_{z^2} orbitals on one Mn^{III} center and the empty $d_{x^2-y^2}$ orbital on a neighboring Mn^{III} center (bottom).

It was possible to fit the experimental values of J using the function of eq 10 (see the plot corresponding to this fit included in Figure 5, left) with negative (positive) best-fit values of $J_0(J_1)$ [−6.90 (28.77) and −10.80 (56.30) cm^{-1} for **I**−**IV** and **V**−**VIII**, respectively]. Using VBCI in the next section, we will justify the choice of the particular form of eq 10 and analyze the parameters J_0 and J_1 in terms of the underlying magnetic interactions involved in the exchange.

$$J = J_0 + J_1 \sin^2 \gamma \qquad (10)$$

III.2. VBCI Model for Magnetic Exchange in the Mn_3 SMM. *III.2.1. Magnetic Exchange across the Mn−O−N−Mn Bridge.* We consider here a Mn−O−N−Mn pair with the

dx.doi.org/10.1021/ic1023482 |*Inorg. Chem.* 2011, 50, 2112–2124

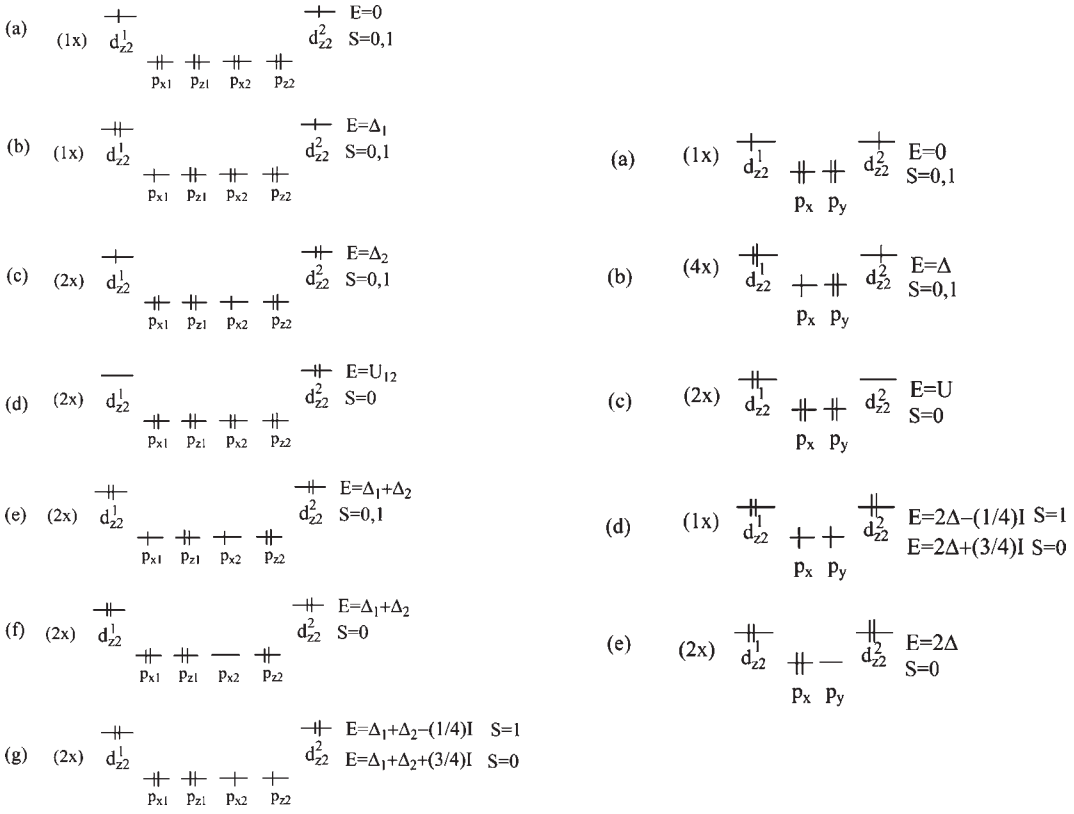

Figure 7. Types of configurations and their zero-order energy expressions included in the VBCI model for exchange via the Mn−O−N−Mn bridge (left) and Mn−O−Mn (right).

bridging geometry shown in Figure 6, top, right. In the Jahn−Teller distorted octahedral Mn^{III} ($t_{2g}^3 e_g^1$) complex, the single e_g^1 electron occupies a σ-antibonding d_{z^2} type molecular orbital, while the three unpaired electrons on t_{2g} are only weakly π-antibonding. In our consideration, we first concentrate on the singly occupied (empty) d_{z^2} ($d_{x^2-y^2}$) orbitals on Mn^{III} and consider the effect of the t_{2g} orbitals in a second step. In the VBCI method, one starts with an ionic configuration consisting of singly occupied $d_{z^2}^1$ and $d_{z^2}^2$ orbitals on Mn_1 and Mn_2 and doubly occupied N and O ligand orbitals (p_x and p_z; Figure 6, top, right). The two unpaired σ electrons give rise to four microstates ($\alpha\beta$, $\beta\alpha$, $\alpha\alpha$, and $\beta\beta$), i.e., to one singlet and one triplet, which are degenerate in a first approximation but can interact (in a different way and therefore can split) with singly (Δ) and doubly (2Δ) ligand-to-metal (LMCT) and metal-to-metal (U, MMCT) charge-transfer excited states (Figure 7, left). The coupling between these configurations is governed by the metal−ligand and intraligand hopping integrals of σ type, expressed in terms of $t_{pd\sigma} = h_{pd\sigma}/2$ ($h_{pd\sigma}$ hopping intergral for a standard orientation), which we set equal for Mn−O and Mn−N interactions), and π type ($t_{pp\pi}$), respectively. In the chosen coordinate frame, we take the Mn_1−N−O fragment as fixed and account for the dihedral Mn_1−N−O−Mn_2 angle rotating the Mn_2−O bond by γ around the O−N bond (Figure 6, top, right). The one-electron matrix elements of eqs 11.1−11.4 (see also Table S3 in the Supporting Information) and spin-adapted wave functions (see Figure 6, top, right, for the coordinate choice and orbital numbering) have been used to set up the 12 × 12 and 8 × 8 matrices (Tables S4 and S5 in the Supporting Information) for the singlet (S) and triplet (T) states.

$$\langle d_{z^2}^1 | \hat{h} | p_x^1 \rangle = t_{pd\sigma} \tag{11.1}$$

$$\langle d_{z^2}^2 | \hat{h} | p_x^2 \rangle = t_{pd\sigma} \cos\gamma \tag{11.2}$$

$$\langle d_{z^2}^2 | \hat{h} | p_z^2 \rangle = t_{pd\sigma} \sin\gamma \tag{11.3}$$

$$\langle p_x^1 | \hat{h} | p_x^2 \rangle = \langle p_z^1 | \hat{h} | p_z^2 \rangle = -t_{pp\pi} \tag{11.4}$$

Perturbation theory up to sixth-order (see the Supporting Information) results in the following expression of J describing the exchange splitting of the S = 2, 1, and 0 Mn^{III}−Mn^{III} pair states:

$$J_{oxime} = E(S=0) - E(S=1) = J_{oxime}^k \cos^2\gamma + J_{oxime}^p \sin^2\gamma \tag{12}$$

$$J_{oxime}^k = -\frac{1}{16}\frac{t_{pd\sigma}{}^4 t_{pp\pi}{}^2}{\Delta^5} \tag{13}$$

$$J_{oxime}^p = \frac{I_{pp}}{40}\frac{t_{pd\sigma}{}^4 t_{pp\pi}{}^2}{\Delta^6} \tag{14}$$

In eq 12, the J_{oxime}^k term accounts for delocalization of the unpaired electrons from one Mn center to a neighboring one; it tends to stabilize a S = 0 pair state and takes a maximum value for a planar Mn−O−N−Mn geometry (γ = 0, kinetic

dx.doi.org/10.1021/ic1023482 |Inorg. Chem. 2011, 50, 2112–2124

exchange). The J^{p}_{oxime}term stems from doubly LMCT excited states, where two electrons with the same spin appear on O or N; the intraligand (Hund) exchange coupling (I_{pp}; potential exchange) then tends to stabilize the $S = 4$ Mn−Mn pair ground state.

Transfer of the spin density from the singly occupied d_{z^2} orbital of $Mn_1(d^4)$ into the empty $d_{x^2-y^2}$ orbital of $Mn_2(d^4)$ (and vice versa) via the bridging ligands (spin polarization, sp) leads to ferromagnetic coupling with contributions from the intraatomic (Hund) exchange coupling energy (I_{dd}); for the Mn^{II} ion with a high-spin d^5 configuration, this energy takes appreciable values (see below). Effects of this type have been analyzed using the VBCI model in cyanide-bridged transition-metal complexes.[26] In order to illustrate the leading term of this interaction, we take a planar Mn−O−N−Mn geometry (Figure 6, bottom, right) and account for the orbital interactions in terms of the hopping integrals of eqs 15.1−15.5 (see Figure 6, bottom right):

$$\langle d^1_{z^2}|\hat{h}|p^1_x\rangle = t_{pd\sigma} \tag{15.1}$$

$$\left\langle d^2_{x^2-y^2}|\hat{h}|p^2_x\right\rangle = -\sqrt{3}t_{pd\sigma} \tag{15.2}$$

$$\langle d^2_{z^2}|\hat{h}|p^2_x\rangle = t_{pd\sigma} \tag{15.3}$$

$$\left\langle d^1_{x^2-y^2}|\hat{h}|p^1_x\right\rangle = -\sqrt{3}t_{pd\sigma} \tag{15.4}$$

$$\langle p^1_x|\hat{h}|p^2_x\rangle = -t_{pp\pi} \tag{15.5}$$

CT excitations from doubly occupied ligand orbitals p^1_x and p^2_x to the empty $d_{z^2-y^2}{}^1$ and $d_{z^2-y^2}{}^1(\Delta)$ and back transfer from the singly occupied $d_{z^2}{}^1$ and $d_{z^2}{}^2$ to the p^1_x and p^2_x orbitals (effectively a CT from Mn_1 to Mn_2 and vice versa, described by the energy U) and their mixing via the matrix elements (15.1)−(15.5) into the ground state have been used to set up the 21 × 21 and 15 × 15 secular problems of the triplet and singlet, respectively. Perturbation theory up to sixth-order (see the Supporting Information) leads to the following contributing to J_{oxime}:

$$J^{sp}_{oxime}(1+\sin^2\gamma) \tag{16}$$

with

$$J^{sp}_{oxime} = \frac{3}{10}\frac{t_{pd\sigma}{}^4 t_{pp\pi}{}^2}{\Delta^4 U}\left(\frac{1}{U}+\frac{4}{\Delta}\right)I_{dd} \tag{17}$$

In eq 16, we account for the contribution of the singly occupied d^1_{xz} and d^2_{xz} orbitals on Mn^{III}. These orbitals are of purely π-type symmetry for planar Mn−O−N−Mn bridges but acquire σ character, which increases with γ (eq 18.118).

$$\langle d^1_{xz}|\hat{h}|p^1_x\rangle = \sqrt{3}t_{pd\sigma}\sin\gamma \tag{18.1}$$

$$\langle d^2_{xz}|\hat{h}|p^2_x\rangle = \sqrt{3}t_{pd\sigma}\sin\gamma \tag{18.2}$$

III.2.2. Magnetic Exchange across the Mn−O−Mn Bridge. Bridging oxide mediates magnetic exchange through its electron pairs $(p_x)^2$ and $(p_y)^2$ involved in σ bonds within the Mn_3 plane and through the out-of-the plane π-type $(p_z)^2$ electron pair, which we neglect in the following. A minimum orbital basis for the problem consists of the fully occupied O p_x and p_y orbitals and the singly occupied Mn^{III} $d_{z^2}{}^1$ and $d_{z^2}{}^2$ orbitals (Figure 6, top, left). Starting with the ground state, singly and doubly LMCT and MMCT excited-state configurations are created (Figure 7, right) . Ligand-to-metal hopping integrals (eqs 19.1 and 19.2 and Table S6 in the Supporting Information) account for the intermixing of these configurations into the ground-state triplet

$$\langle d^1_{z^2}|\hat{h}|p_x\rangle = -\langle d^2_{z^2}|\hat{h}|p_x\rangle = -t_{pd\sigma}\sin(\alpha/2) \tag{19.1}$$

$$\left\langle d^1_{z^2}|\hat{h}|p_y\right\rangle = \left\langle d^2_{z^2}|\hat{h}|p_y\right\rangle = -t_{pd\sigma}\cos(\alpha/2) \tag{19.2}$$

(T) or singlet (S) states and lead to stabilization of one of these states with respect to the other depending on the Mn−O−Mn angle α. The secular problems are of dimensions 6 × 6 (for T) and 10 × 10 (for S). Fourth-order perturbation theory leads to eq 20 for the exchange coupling parameter J_{oxide} with contributions from kinetic (J^{k}_{oxide}; eq 21) and potential (J^{p}_{oxide}; eq 22) exchange coupling (eq 20). In eq 20, we also account for the spin-polarization term J^{sp}_{oxide} (eq 23) originating from CT excitation from the singly occupied d_{z^2} orbitals of one Mn center into the empty $d_{x^2-y^2}$ orbitals of a neighboring one (see the Supporting Information and Mathematica programs of its derivation).

$$J_{oxide} = E(S=0) - E(S=2) = (J^{k}_{oxide} + J^{sp}_{oxide})\cos^2\alpha + J^{p}_{oxide}\sin^2\alpha \tag{20}$$

$$J^{k}_{oxide} = -\frac{1}{4}\frac{t_{pd\sigma}{}^4}{\Delta^2}\left(\frac{1}{\Delta}+\frac{1}{U}\right) \tag{21}$$

$$J^{p}_{oxide} = \frac{I_{pp}}{80}\frac{t_{pd\sigma}{}^4}{\Delta^4} \tag{22}$$

$$J^{sp}_{oxide} = \frac{3}{10}\frac{t_{pd\sigma}{}^4}{U\Delta^2}\left(\frac{1}{U}+\frac{2}{\Delta}\right)I_{dd} \tag{23}$$

Given the relationship between the α and θ angles (eq 24), one obtains the dependence of J_{oxide} on $\delta\theta$ (eq 25). Based on the very small experimentally reported values of $\delta\theta$ and the particular form of the dependence on $\delta\theta$ (eq 25), the magnetic exchange coupling via the Mn−O−Mn angle is found by VBCI to weakly depend on the angle $\delta\theta$ being dominated mostly by the term $J^{k}_{oxide} + J^{sp}_{oxide}$ (see the next section).

$$\sin(\alpha/2) = \left(\frac{\sqrt{3}}{2}\right)\sin\theta; \quad \delta\theta = 90-\theta \tag{24}$$

$$J_{oxide} = J^{k}_{oxide} + J^{sp}_{oxide} + 3(J^{p}_{oxide} - J^{k}_{oxide} - J^{sp}_{oxide})\cos^2\delta\theta\left(1-\frac{3}{4}\cos^2\delta\theta\right) \tag{25}$$

III.2.3. Estimation of the Parameters of the VBCI Model and Comparison with the Experiment and DFT Results. Summarizing the various contributions to the exchange from the oximato and oxide bridges (eqs 12, 16, and 20), we can write down the exchange coupling energy of a Mn−Mn pair J in the form given by eq 26.1. From a comparison with eq 10, we can then decompose the

$$J = (J^{k}_{oxide} + J^{sp}_{oxide})/4 + 3J^{p}_{oxide}/4 + J^{k}_{oxime} + J^{sp}_{oxime} + (J^{p}_{oxime} - J^{k}_{oxime} + J^{sp}_{oxime})\sin^2\gamma \tag{26.1}$$

dx.doi.org/10.1021/ic1023482 |Inorg. Chem. 2011, 50, 2112–2124

$$J_0 = (J^k_{oxide} + J^{sp}_{oxide})/4 + 3J^p_{oxide}/4 + J^k_{oxime} + J^{sp}_{oxime} \quad (26.2)$$

$$J_1 = J^p_{oxime} - J^k_{oxime} + J^{sp}_{oxime} \quad (26.3)$$

energies J_0 and J_1 in terms of the exchange coupling terms of eqs 26.2 and 26.3 and evaluate their values based on the VBCI expressions (eqs 13, 14, 17, and 21−23). To this end, a brief discussion of the VBCI model parameters and their magnitudes is in order. The CT energy U, defined as the difference between the one-center (γ_{11}) and two-center (γ_{12}) d−d repulsion integrals, can be calculated from the Racah parameter B, obtained from optical d−d spectra (B = 760 cm^{-1} [56] and the Mn−Mn distance (R_{Mn-Mn} = 3.246 Å), assuming a simple Coulomb law of two-center interelectronic repulsion (eq 27).[57] The LMCT spectrum of Mn^{IV} doped in corundum Al_2O_3 shows a peak position at 33 000 cm^{-1}, which has been assigned as being due to Mn^{III} as an impurity.[58] On the basis of the same work,

$$U = \gamma_{11} - \gamma_{12} = 146B - 116165/R_{Mn-Mn} \quad (27)$$

a value of Δ for the isovalent Cr^{III} in the 42 000−56 000 cm^{-1} range has been adopted in VBCI analysis of the exchange coupling of Cr^{III} in $[(NH_3)_5CrOCr(NH_3)_5]^{4+}$ (basis rodo salt), yielding J in good agreement with the experiment.[59] Given the shift of the 3d orbitals by 10 700 cm^{-1} [60] to lower energies when going from Cr^{III} to Mn^{III}, we adopt here a value of Δ (Mn^{III}) in the range of 31 000−45 000 cm^{-1}. From Δ and the reported spectroscopic value of the parameter e_σ (the average antibonding energy due to equatorial N and O ligands, e_σ = 9500 cm^{-1} [56]), the hopping integral $t_{pd\sigma}$ has been deduced using eq 28, given by the angular overlap model, which relates e_σ, $t_{pd\sigma}$ = $h_{pd\sigma}/2$, and Δ. No spectroscopic data are available thus far that would allow one to obtain the intraligand hopping parameter $t_{pp\pi}$; the value that we adopt here ($t_{pp\pi}$ = 19 765 cm^{-1}) was deduced from a DFT calculation on the free ligand making use of the KS eigenvalues and eigenvectors used to reconstruct the one-electron matrix elements (eqs S.3−S.6 in the Supporting Information).

$$e_\sigma = \frac{h_{pd\sigma}{}^2}{\Delta} = \frac{4t_{pd\sigma}{}^2}{\Delta} \quad (28)$$

A value of the parameter I_{pp} of the intraligand exchange (−5000 cm^{-1}) has been deduced using data on atomic spectra of O.[61] Finally, the parameter of Mn^{II} intraatomic exchange I_{dd} has been expressed as given in eq 29, with $I = [C + (5/2)B]$,

$$I_{dd} = 5I \quad (29)$$

an average one-center two-electron exchange integral and the prefactor 5, the number of unpaired d electrons.[62] Again, we use here spectroscopic data for the Racah parameters B and C (B = 760 cm^{-1} and C = 3290 cm^{-1}) to obtain the value I_{dd}.

With the set of VBCI parameters (Table 3), now it is possible to obtain an estimate of the various contributions to the exchange coupling energy listed in Table 4. Because of intraatomic Hund exchange, CT from the doubly occupied bridging ligand to the empty $d_{x^2-y^2}$ orbitals of Mn^{III} leads to a spin density on these orbitals of the same sign, leaving a negative spin density both on the N−O oximato bridge and on the μ_3-O as well. Because overlap of the σ type between ligand orbitals is larger for $d_{x^2-y^2}$ than for d_{z^2}, this spin-polarization mechanism dominates the Mn−O−N−Mn exchange. For the extended Mn−O−N−Mn bridge, this interaction leads to ferromagnetic coupling, with the

Table 3. Parameter Values (cm^{-1}) of the VBCI Model

$t_{pd\sigma}$	t_{pp}	Δ	U	I_{dd}	I_{pp}
9460 ± 880	19 765	38 000 ± 7000	75 000	25 950	5000

Table 4. Antiferromagnetic (J^k) and Ferromagnetic (J^p, J^{sp}) Contributions (cm^{-1}) to the Exchange Coupling Energy of a Mn−Mn Pair for the Oximate (J_{oxime}) and Oxide (J_{oxide}) Bridge as Given by the VBCI Model[a]

J^k_{oxime}	J^p_{oxime}	J^{sp}_{oxime}	J^k_{oxide}	J^p_{oxide}	J^{sp}_{oxide}
−3.06 ± 1.56	0.18 ± 0.12	22.72 ± 11.16	−57.22 ± 7.08	0.27 ± 0.10	39.70 ± 5.88

[a] Calculated with the parameter set of Table 3.

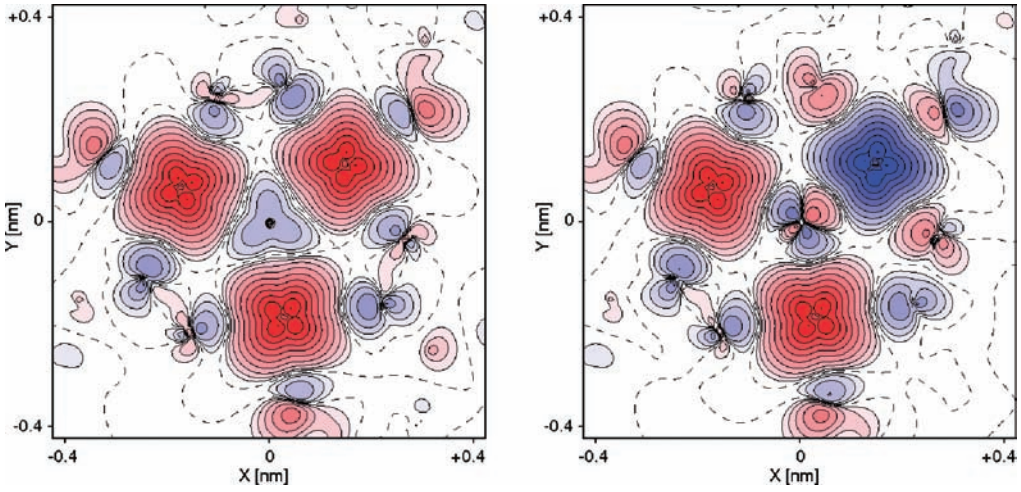

Figure 8. Spin-density maps for $[Mn^{III}_3O(Me\text{-}sao)_3(2,4'\text{-}bpy)_3ClO_4]$ within the Mn_3 plane from S = 6 high-spin (left) and M_s = 2 broken-spin (right) DFT calculations.

dx.doi.org/10.1021/ic1023482 |Inorg. Chem. 2011, 50, 2112–2124

leading term J^{sp}_{oxime} (Table 4) determining both the sign and angular dependence ($\sim\sin^2\gamma$) of J. A similar observation, ferromagnetic coupling with important contributions from spin polarization, was deduced from analysis of the Cu−N−C−Fe bond in CuFe and Cu_2Fe complexes.[40,63] In a strong support of this interpretation, spin-density plots (Figure 8) show negative spin density both on the oximato N and O bridging atoms and, interestingly enough, also on the μ_3-oxide bridging ligand. The dominating ferromagnetic exchange across the oximato bridge is strongly supported by DFT calculations on Mn_3O model clusters, where we replaced μ-O by μ-Ne, thus suppressing contributions from the Mn−O_{oxo}−Mn bridge (Table S9 in the Supporting Information). The results show that the Mn−O−N−Mn exchange energy J is always positive, ranging from about 7 cm^{-1} ($\gamma = 0$) to 61 cm^{-1} ($\gamma = 45°$) and does not depend on the particular value of $\delta\theta$.

As follows from the data in Table 4, the exchange coupling via the Mn−O−Mn bridge is dominated by the negative kinetic term $J^{k}_{oxide} = -57.22 \pm 7.08$ cm^{-1}, which is, however, largely reduced by the rather significant ferromagnetic term $J^{sp}_{oxide} = 39.70 \pm 5.88$ cm^{-1}. As a result, the overall exchange coupling via the oxide bridge is weak and antiferromagnetic and yields the leading contribution to the negative value of J_o, deduced from a best fit to experiment. In contrast, J_1 is positive and dominated by J^{sp}_{oxime}. The comparison between the experimental and theoretical values of J_1 demonstrates the ability of both DFT and VBCI to reproduce the correlation between J and γ (Table 5). In contrast, antiferromagnetic contributions to J_0 are exaggerated by DFT but are outweighed by spin-polarization effects in the VBCI, leading to a positive J_0.

Thus far, we ignored effects on J due to variations of $\delta\theta$. As follows from the contour plot diagram (Figure 4), these variations are still significant but do not follow the prediction of the simple VBCI model in the whole range of γ values. Thus, for large angles γ, both DFT and experiment[64] show that ferromagnetic coupling becomes weaker when $\delta\theta$ increases, in agreement with eq 25 given by the VBCI model. However, for regions with small angles γ, where the overall J is antiferromagnetic, out-of-plane shifts of the oxo anion beyond a critical value of $\delta\theta \sim 3-4°$ lead to lower $|J|$ values, in agreement with earlier suggestions.[15] As a result, both the $J(\gamma)$ curves for $\delta\theta = 0.6°$ and 7.8° from DFT and the ones given by the fit of the experimental data using eq 10 (Figure 5, left) cross at intermediate values of γ. Apparently, such tiny effects are beyond the reach of the simple VBCI model.

Table 5. Parameters J_0 and J_1 of the Exchange Coupling Energy of a Mn−Mn Pair $J = J_0 + J_1 \sin^2\gamma$ As Derived from a Fit to the Experimental and DFT Data and Calculated with the VBCI Model (Equations 26.2 and 26.3)

	exptl			
	I−IV	V−VIII	DFT	VBCI
J_0	−6.90	−10.88	-12.74 ± 0.72[a]	15.48 ± 9.38[b]
J_1	28.77	56.30	44.97 ± 4.61[a]	25.96 ± 12.84[b]
standard deviation	0.48	0.50	0.89 ± 0.25	

[a] Best-fit parameters to $J(\gamma)$ dependencies employing values of $\delta\theta = 0.6°$ (upper sign) and $\delta\theta = 7.8°$ (lower sign). See Figure 5 for a comparison between J vs γ plots from DFT and those calculated using eq 10 with the parameters J_0 and J_1 obtained from a best fit. [b] Calculated with the set of parameters listed in Tables 3 and 4.

III.3. Magnetostructural Correlations and Exchange Mechanism in the Mn_6-Based SMM. Let us consider now the exchange coupling in Mn_6 SMM in light of the results of the preceding section. The 24 complexes of this family fall into two general categories, $[Mn^{III}_6O_2(R\text{-sao})_6X_2sol_4]$ and $[Mn^{III}_6O_2(R\text{-sao})_6X_2sol_{5,6}]$, as a consequence of the distortion imparted on the $[Mn^{III}_6O_2(N-O)_6]$ by the bulky alkyl substituents R. In four of the members (R = H), the two carboxylate ligands X are bridging one Mn^{III}−Mn^{III} pair of each Mn_3 triangle [Mn(2) and Mn(3); see Figure 1 for the numbering), while in the other molecules (R = CH_3, C_2H_5), this ligand is terminal, i.e., bound to Mn(3), and the coordination sphere of Mn(2) is completed by

Table 6. Broken-Symmetry DFT Values of the Exchange Coupling Energies between Pairs of Mn^{III} Ions in Selected Members of the Mn_6 SMM Family, Calculated Directly Using Geometries from X-ray Diffraction Data and the B3LYP (J_{B3LYP}) Exchange-Correlation Potentials Estimated Using the $J(\gamma,\delta\theta)$ Correlation Function (eq 7 and Table S2 in the Supporting Information) (J^{corr}_{B3LYP}) and the γ and $\delta\theta$ Angles[a]

compd no.[a]	γ_{12}	γ_{13}	γ_{23}	$\delta\theta$	J	J_{12}	J_{13}	J_{23}[c]	$J_{33'}$	J_{ph}	ref
1	10.4	25.6	18.0	6.9	J_{B3LYP}	−6.2	2.6	−21.0	5.8	−1	*b*
					J^{corr}_{B3LYP}	−13.0	−5.8	−10.2			this study
2	25.5	29.7	42.4	2.3	J_{B3LYP}	−3.0	−3.2	2.4	6.4	−1.6	*b*
					J^{corr}_{B3LYP}	−3.6	−0.4	8.5			this study
4	31.8	23.8	47.6	1.9	J_{B3LYP}	1.6	−6.8	6.2	6.2	−0.4	*b*
					J^{corr}_{B3LYP}	1.6	−4.5	11.6			this study
8	39.1	34.9	43.0	1.0	J_{B3LYP}	5.2	3.2	2.4	6.2	1.0	*b*
					J^{corr}_{B3LYP}	7.9	4.9	10.4			this study
10	27.4	36.4	31.1	1.0	J_{B3LYP}	−3.6	4.6	−4.6	4.2	−1.4	*b*
					J^{corr}_{B3LYP}	−0.8	6.0	2.1			this study
12	27.8	40.1	41.5	3.1	J_{B3LYP}	−1.8	5.8	0.0	6.6	0.0	*b*
					J^{corr}_{B3LYP}	−2.6	6.3	7.1			this study

[a] The numbering of the complexes follows the notations adopted in ref 11, i.e., $[Mn_6O_2(H\text{-sao})_6(O_2CH)_2(MeOH)_4]$ (**1**), $[Mn_6O_2(Me\text{-sao})_6(O_2CCPh_3)_2(EtOH)_4]$ (**2**), $[Mn_6O_2(Et\text{-sao})_6(O_2CPh^2OPh)_2(EtOH)_4]$ (**4**), $[Mn_6O_2(Et\text{-sao})_6\{O_2CPh(Me)_2\}_2(EtOH)_6]$ (**8**), $[Mn_6O_2(Me\text{-sao})_6(O_2C\text{-th})_2(EtOH)_4(H_2O)_2]$ (**10**), and $[Mn_6O_2(Et\text{-sao})_6(O_2C_{12}H_{17})_2(EtOH)_4(H_2O)_2]$ (**12**). [b] Reference 14; the numbering of the Mn centers (γ angles) in this reference (*i*) are related with the ones adopted by us (Figure 1); (*j*) as $j \rightarrow i$, $1 \rightarrow 2$, $2 \rightarrow 3$, $3 \rightarrow 1$. [c] Exchange coupling parameter for the Mn−N−O−Mn bridge with oxime O donors linking the two Mn_3 triangles.

dx.doi.org/10.1021/ic1023482 |*Inorg. Chem.* 2011, 50, 2112–2124

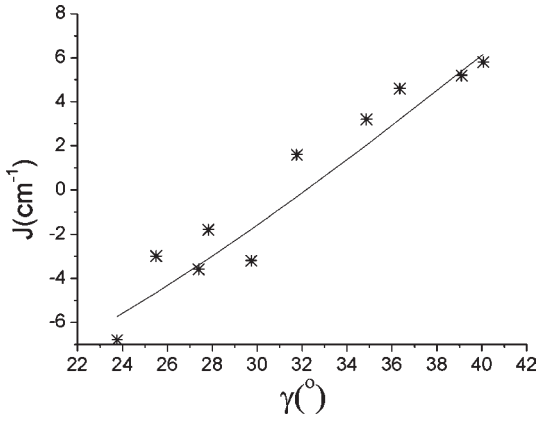

Figure 9. Magnetostructural correlations of the values of J for the Mn−Mn pairs with oximato and oxide double bridges derived from the reported B3LYP values (ref14, crosses) and best fit (eq 10) with $J = -13.4 + 47.2 \sin^2 \gamma$ (straight line).

one or two additional solvent molecules (sol). Because of the rather low symmetry of each Mn_3 moiety, reflected in different values of the γ angles γ_{12}, γ_{13}, and γ_{23} (see Figure 1), and the additional linking of the triangles via oximato and phenolato O atoms, five different exchange coupling parameters were introduced to describe the magnetic exchange.[14] In ref.[14] DFT (B3LYP) calculations have been employed to deduce all model parameters J; in Table 6, we list their values along with the corresponding γ_{12}, γ_{13}, γ_{23}, and $\delta\theta$ angles taken from the experiment.

The exchange coupling parameters in Table 6 have been successfully applied and found to reproduce magnetic susceptibility curves reasonably well.[14] The parameters J_{12} and J_{13} pertain to exchange pathways through double oxo−oximato bridging ligands, and therefore they can be compared with the results obtained independently for Mn_3 SMM (see the preceding section). Because of the bridging function that the HCO_2^- ligand takes in complex **1**, we exclude this complex from the comparison, and, further, because of the μ_3 type of bridging of the oxime O coordinated to Mn(3) [Mn(3′)] linking the two Mn_3 units, we discard in our analysis also the parameter J_{23}. We should further note that, for the systems under consideration, the angles $\delta\theta$ do not vary largely, such that in a good approximation we can apply eq 10 to correlate values of J_{12} and J_{13} with the corresponding γ angles (Figure 9). A least-squares fit leads to the parameter values $J_0 = -13.4$ cm^{-1} and $J_1 = 47.2$ cm^{-1}, which are consistent with the values that we deduce independently from the experimental susceptibility data on the Mn_3 compounds (−10.8 and 56.3 cm^{-1}; Table 5) and with the DFT values (eq 7; $J_0 = -12.74$ cm^{-1} and $J_1 = 44.97$ cm^{-1}), with all compounds possessing the same type of bridging geometry but different constitution. This shows that, allowing for the dependence on the detailed value of J on the angles γ and $\delta\theta$, the parameters J are fairly well transferable from the trigonal Mn_3 to the less symmetric Mn_6 molecules and this justifies the use of the DFT results (eq 7) for predictive purposes, allowing one to deduce J for Mn−O−N−Mn exchange-coupled pairs in less symmetric molecules, with known geometries given by γ and $\delta\theta$. In the same context, one should also notice that the magic value of $\gamma = 30°$, for which experimentally it was found that J switches from positive to negative values upon an increase of γ, is nicely reproduced by the contour plots of Figure 4.

IV. CONCLUSIONS

1 Using the VBCI model and perturbation theory, analytical expressions of the exchange coupling energy J of the Mn_3 SMM depending on angular distortions, the torsion angle γ (eqs 12−14, 16, and 17), and the out-of-plane shift angle $\delta\theta$ (eqs 21−23 and 25) have been derived. Ferromagnetic exchange interactions in these magnetic clusters are found both by DFT and VBCI to be governed by a spin-polarization mechanism (Figure 8) with dominant ferromagnetic exchange via the oximato bridge and by kinetic exchange, leading to a weaker antiferromagnetic spin coupling via the oxide bridge.

2 A series of DFT geometry optimizations constraining the angles γ and $\delta\theta$ allows one to map the rather complex dependence of J on the bridging geometry onto γ and $\delta\theta$, showing that J undergoes larger influences because of variation of the twist angle γ and smaller ones due to $\delta\theta$ (Figures 4, right, and 5). This supports conclusions from earlier studies based on both the experiment and theory. Contour plot diagrams of J depending on the γ and $\delta\theta$ angles calculated using the B3LYP functional are found to perfectly match the experimental values of J deduced from magnetic susceptibility data on a Mn_3 SMM (Figure 4).

3 The results have been applied and validated using a Mn_6 SMM to show that exchange coupling parameters J are well transferable from the Mn_3 trigonal to the low-symmetric Mn_6 SMM magnetic clusters when making allowance for variation of J with γ and $\delta\theta$ (Figure 9).

4 A GGA functional for magnetic exchange developed in our group (DB97) has been found to reproduce ferromagnetic exchange coupling constants with remarkable success, with results being comparable with those obtained when using the popular but computationally more demanding B3LYP functional. However, antiferromagnetic exchange coupling is overestimated also by the DB97 XCP, a situation common to all GGA functionals.

■ ASSOCIATED CONTENT

Supporting Information. Exchange coupling energies, coefficients of the J vs $(\gamma, \delta\theta)$ polynomial, orbital manifold and hopping integrals, matrix for triplets and of singlets, $(d_{x^2-y^2}{}^0 - d_{z^2}{}^1)$ exchange pathways, section on deducing hopping integrals from DFT, contour plot diagrams (Figures S1−S6), and a zip file. This material is available free of charge via the Internet at http://pubs.acs.org.

■ AUTHOR INFORMATION

Corresponding Author

*E-mail: bernard.delley@psi.ch (B.D.), mihail.atanasov@aci.uni-heidelberg.de (M.A.), neese@thch.uni-bonn.de (F.N.).

Notes

‖It is with great sadness that we report the death of Philip Louis William Tregenna-Piggott (Feb 26, 2010), the initiator and supporter of the present work, the enthusiast and dreamer, our good friend.

■ ACKNOWLEDGMENT

The authors thank the Swiss National Foundation and the Paul Scherrer Institute for a research grant (to M.A.), which

made this study possible. Thanks are due to the Deutsche Forschungsgemeinschaft for the SFB 813 Program "Chemistry on Spin Centers", which allowed us to finalize this work.

REFERENCES

(1) Caneschi, A.; Gatteschi, D.; Sessoli, R.; Barra, A. L.; Brunel, L. C.; Guillot, M. *J. Am. Chem. Soc.* **1991**, *113*, 5873.

(2) Sessoli, R.; Gatteschi, D.; Caneschi, A.; Novak, M. A. *Nature* **1993**, *365*, 141.

(3) Gatteschi, D.; Sessoli, R. *Angew. Chem., Int. Ed.* **2003**, *42*, 246.

(4) Gatteschi, D.; Sessoli, R.; Villian, J. *Molecular Nanomagnets*; Oxford University Press: Oxford, U.K., 2006.

(5) Screerama, S. G.; Pal, S. *Inorg. Chem.* **2002**, *41*, 4843.

(6) Stamatatos, T. C.; Foguet-Albiol, D.; Stoumpos, C. C.; Raptopoulou, C. P.; Terzis, A.; Wernsdorfer, W.; Perlepes, S. P.; Christou, G. *J. Am. Chem. Soc.* **2005**, *127*, 15380–15381.

(7) Stamatatos, T. C.; Foguet-Albiol, D.; Stoumpos, C. C.; Raptopoulou, C. P.; Terzis, A.; Wernsdorfer, W.; Perlepes, S. P.; Christou, G. *Polyhedron* **2007**, *26*, 2165–2168.

(8) Stamatatos, T. C.; Foguet-Albiol, D.; Lee, S.-C.; Stoumpos, C. C.; Raptopoulou, C. P.; Terzis, A.; Wernsdorfer, W.; Hill, S. O.; Perlepes, S. P.; Christou, G. *J. Am. Chem. Soc.* **2007**, *129*, 9484–9499.

(9) Milios, C. J.; Vinslava, A.; Wood, P. A.; Parsons, S.; Wernsdorfer, W.; Christou, G.; Perlepes, S. P.; Brechin, E. K. *J. Am. Chem. Soc.* **2007**, *129*, 8–9.

(10) Milios, C. J.; Vinslava, A.; Wernsdorfer, W.; Moggach, S.; Parsons, S.; Perlepes, S. P.; Christou, G.; Brechin, E. K. *J. Am. Chem. Soc.* **2007**, *129*, 2754–2755.

(11) Milios, C. J.; Inglis, R.; Vinslava, A.; Bagai, R.; Wernsdorfer, W.; Parsons, S.; Perlepes, S. P.; Christou, G.; Brechin, E. K. *J. Am. Chem. Soc.* **2007**, *129*, 12505–12511.

(12) Inglis, R.; Jones, L. F.; Milios, C. J.; Datta, S.; Collins, A.; Parsons, S.; Wernsdorfer, W.; Hill, S.; Perlepes, S. P.; Piligkos, S.; Brechin, E. K. *Dalton Trans.* **2009**, 3403–3412 and references cited therein.

(13) Inglis, R.; Taylor, S. M.; Jones, L. F.; Papaefstathiou, G. S.; Perlepes, S. P.; Datta, S.; Hill, S.; Wernsdorfer, W.; Brechin, E. K. *Dalton Trans.* **2009**, 9157.

(14) Cremades, E.; Cano, J.; Ruiz, E.; Rajaraman, G.; Milios, C. J.; Brechin, E. K. *Inorg. Chem.* **2009**, *48*, 8012–8019.

(15) Cano, J.; Cauchy, T.; Ruiz, E.; Milios, C. J.; Stoumpos, C. C.; Stamatatos, T. C.; Perlepes, S. P.; Christou, G.; Brechin, E. K. *Dalton Trans.* **2008**, 234–240. Deviations of O_{oxide} from Mn_3 have been defined in terms of the shift distance d measured in angstroms in this and later papers (refs 13, 32−34). Because the $Mn-O_{oxide}$ distances remain almost unchanged, there is a one-to-one correspondence of the two parameters, given by $\delta\theta$ (deg) = $180d/\pi R$.

(16) Zhang, Y.-Q.; Luo, C.-L. *Dalton Trans.* **2009**, 5627–5636.

(17) Cirera, J.; Ruiz, E.; Alvarez, S.; Neese, F.; Kortus, J. *Chem.—Eur. J.* **2009**, *15*, 4078–4087.

(18) (a) Pantazis, D. A.; Orio, M.; Petrenko, T.; Zein, S.; Bill, E.; Lubitz, W.; Messinger, J.; Neese, F. *Chem.—Eur. J.* **2009**, *15*, 5108. (b) Orio, M.; Pantazis, D. A.; Petrenko, T.; Neese, F. *Inorg. Chem.* **2009**, *48*, 7251.

(19) Romain, S.; Duboc, C.; Neese, F.; Revière, E.; Hanton, L. R.; Blackman, A. G.; Philouze, C.; Leprêtre, J.-C.; Deronzier, A.; Collomb, M.-N. *Chem.—Eur. J.* **2009**, *15*, 980.

(20) Duboc, C.; Ganyushin, D.; Sivalingam, K.; Cullomb, M.-N.; Neese, F. *J. Phys. Chem. A* **2010**, *114*, 10750.

(21) Pantazis, D. A.; Krewald, V.; Orio, M.; Neese, F. *Dalton Trans.* **2010**, *39*, 4959.

(22) Oshio, H.; Nakano, M. *Chem.—Eur. J.* **2005**, *11*, 5178.

(23) Piligkos, S.; Bendix, J.; Weihe, H.; Milios, C. J.; Brechin, E. K. *Dalton Trans.* **2008**, 2277.

(24) Zaanen, J.; Sawatzky, G. A. *Can. J. Phys.* **1987**, *65*, 1262.

(25) Didziulis, S. V.; Cohen, S. L.; Gewirth, A. A.; Solomon, E. I. *J. Am. Chem. Soc.* **1988**, *110*, 250.

(26) Weihe, H.; Güdel, H. U. *Comments Inorg. Chem.* **2000**, *22*, 75.

(27) Tuczek, F.; Solomon, E. I. *Inorg. Chem.* **1993**, *32*, 2850.

(28) Brown, C. A.; Remar, G. J.; Musselmann, R. L.; Solomon, E. I. *Inorg. Chem.* **1995**, *34*, 688.

(29) Tuczek, F.; Solomon, E. I. *Coord. Chem. Rev.* **2001**, *219−221*, 1075.

(30) Tuczek, F.; Solomon, E. I. In *Comprehensive Coordination Chemistry II*; Lever, A. B. P., Ed.; Elsevier: New York, 2003; Vol. 2, p 541.

(31) A theoretical analysis of the magnetic exchange coupling and magnetic anisotropy of the $[Mn^{III}_3O(O_2CR)_3(mpko)_3](ClO_4)$ (mpkoH = 2-pyridyl ketone oxime) complex possessing trigonal symmetry has been performed in: Stamatos, T. C.; Foguett-Albiol, D.; Lee, S. C.; Stoumpos, C. C.; Raptopoulou, C. P.; Terzis, A.; Wernsdorfer, W.; Hill, S. O.; Perlepes, S. P.; Christou, G. *J. Am. Chem. Soc.* **2007**, *129*, 9484. However, because of some essential differences between the two families sao-R and mpko-R as to the different coordinations of the bridging ligand (the presence of carboxylato bridging ligands), a direct comparison between them is not feasible.

(32) Yang, C.-I.; Wernsdorfer, W.; Cheng, K.-H.; Nakano, M.; Lee, G.-H.; Tsai, H.-L. *Inorg. Chem.* **2008**, *47*, 10184.

(33) Milios, C. J.; Inglis, R.; Jones, L. F.; Prescimone, A.; Parsons, S.; Wernsdorfer, W.; Brechin, E. K. *Dalton Trans.* **2009**, 2812.

(34) Feng, P. L.; Koo, C.; Henderson, J. J.; Manning, P.; Nakano, M.; del Barco, E.; Hill, S.; Hendrickson, D. N. *Inorg. Chem.* **2009**, *48*, 3480.

(35) Delley, B. *J. Chem. Phys.* **1990**, *92*, 508.

(36) Kohn, W.; Sham, L. J. *Phys. Rev.* **1965**, *140*, A1133.

(37) Perdew, J. P.; Burke, K.; Ernzerhof, M. *Phys. Rev. Lett.* **1996**, *77*, 3865.

(38) Perdew, J. P.; Wang, Y. *Phys. Rev. B* **1992**, *45*, 13244.

(39) Vosko, S. H.; Wilk, L.; Nusair, M. *Can. J. Phys.* **1980**, *58*, 1200.

(40) Atanasov, M.; Comba, P.; Daul, C. A. *Inorg. Chem.* **2008**, *47*, 2449.

(41) Atanasov, M.; Comba,P. in "*The Jahn-Teller Effect:Advances and Perspectives*", Eds Köppel,H.; Barentzen, D. R.; Yarkony, D. R.; Berlin, 2009 p621−650.

(42) Atanasov, M.; Comba, P. In *Structure and Function*; Comba, P., Ed.; Springer: New York, 2010; pp 53−85.

(43) Bühl, M.; Reimann, C.; Pantazis, D. A.; Bredow, T.; Neese, F. *J. Chem. Theory Comput.* **2008**, *4*, 1449.

(44) Kossmann, S.; Neese, F. *J. Chem. Theory Comput.* **2010**, *6*, 2335.

(45) Becke, A. D. *J. Chem. Phys.* **1993**, *98*, 1372; *ibid.* **1993**, *98*, 5648.

(46) Neese, F. *ORCA—An Ab Initio, Density Functional and Semiemprical Program Package*, version 2.6-35; Becker, U.; Ganyushin, D.; Hansen, A.; Liakos, D. G.; Kollmar, C.; Kossmann, S.; Petrenko, T.; Reimann, C.; Riplinger, C.; Sivalingam, K.; Valeev, E.; Wennmohs, F.; Wezisla, B., Contributors; Lehrstuhl für Theoretische Chemie: Bonn, Germany, Feb 2007.

(47) Klamt, A.; Schüürman, G. *J. Chem. Soc., Perkin Trans.* **1993**, *2*, 799.

(48) Neese, F.; Wennmohs, F.; Hansen, A.; Becker, U. *Chem. Phys.* **2009**, *356*, 98.

(49) Neese, F. *J. Comput. Chem.* **2003**, *24*, 1740.

(50) Friesner, R. A. *Chem. Phys. Lett.* **1985**, *116*, 39.

(51) Schäfer, A.; Horn, H.; Ahlrichs, R. *J. Chem. Phys.* **1992**, *97*, 2571.

(52) The Ahlrichs auxiliary basis sets (for density fitting) were obtained from the *Turbomole* basis set library under ftp.chemie.uni-karlsruhe.de/pub/jbasen. Eichkorn, K.;Treutler, O.; Ohm, H.; Haser, M; Ahlrichs, R. *Chem. Phys. Lett.*, **1995**, *240*, 283. Eichkorn, K.; Weigend, F.; Treutler, O.; Ahlrichs, R. *Theor. Chem. Acc.* **1997**, *97*, 119.

(53) Noodleman, L. *J. Chem. Phys.* **1981**, *74*, 5737.

(54) Noodleman, L.; Davidson, E. R. *Chem. Phys.* **1986**, *109*, 131.

(55) Kambe, K. *J. Phys. Soc. Jpn.* **1950**, *5*, 48.

(56) Scheifele, Q.; Riplinger, C.; Neese, F.; Weihe, H.; Barra, A.-L.; Juranyi, F.; Podlesnyak, A.; Tregenna-Piggott, P. L. *Inorg. Chem.* **2008**, *47*, 439.

(57) Atanasov, M.; Angelov, S. *Chem. Phys.* **1991**, *150*, 383.

(58) Tippins, H. H. *Phys. Rev. B* **1970**, *1*, 126.

(59) Weihe, H.; Güdel, H. U.; Toftlund, H. *Inorg. Chem.* **2000**, *39*, 1351.
(60) Harrison, W. A. *Electronic Structure and the Properties of Solids, The Physics of the Chemical Bond*; Freeman: San Francisco, CA, 1980.
(61) Pople, J. A.; Beweridge, D. L. *Approximate Molecular Orbital Theory*; McGraw-Hill: New York, 1970.
(62) Mossin, S.; Weihe, H. *Struct. Bonding (Berlin)* **2004**, *106*, 173–180.
(63) Atanasov, M.; Busche, C.; Comba, P.; El Hallak, F.; Martin, B.; Rajaraman, G.; van Slageren, J.; Wadepohl, H. *Inorg. Chem.* **2008**, *47*, 8112.
(64) One may argue that the specific shifts of the correlation plots for **I**−**IV** and **V**−**VIII** (Figure 5, left) may be due to the different Mn_3 charges, 0 and 3−, respectively. However, calculations with a charge-compensating polarizable continuum within the COSMO model show that this is not the case (cf. Table 2).